


Effect of tilt angle for conical pin tool with a conical shoulder on heat transfer and material flow using numerical simulation in friction stir welding

Amit Yadav  , Ajai Jain, Rajiv Verma

National Institute of Technology Kurukshetra, Kurukshetra, India

 amit.insan77@gmail.com

Abstract. The weld quality is determined by the produced temperature and material flow along the cross-section of the workpiece. In this investigation, a computational fluid dynamics (CFD) model is employed to numerically simulate the heat transfer and material flow of Aluminum alloy AA6061. A conical pin tool with the conical shoulder (CPCS) at different tool tilt angles is considered for a lap joint. Temperature and velocity contours lines are used to study its gradient at different tool tilt angles. The result indicates that higher temperature is generated on trailing advancing side (AS), a high temperature gradient on leading side, and temperature decreases from top to bottom surface along the workpiece thickness. At transverse plane, temperature contour lines lean more towards the advancing side as tilt angle is increased. For CPCS tool, influence of tilt angle on velocity magnitude is negligible. Material from leading AS and front of the tool is observed to be swept along the retreating side (RS) and deposited at the rear of the tool. It is also observed that when tool tilt angle increases, streamlines tend to become more dispersed. It can be deduced that for CPCS, if the tilt angle of the tool is raised, the peak temperature will likewise increase, but the peak material velocity will remain the same. The outcomes of the current investigation are validated by comparison to previously published data. With the above findings and conclusions in mind, CPCS welders can better understand the impact of tool tilt angle on weld quality.

Keywords: Friction Stir Welding, Computational Fluid Dynamics, Fluent, Finite Volume Method

Citation: Yadav A, Jain A, Verma R. Effect of tilt angle for conical pin tool with a conical shoulder on heat transfer and material flow using numerical simulation in friction stir welding. *Materials Physics and Mechanics*. 2023;51(3): 126-145. DOI: 10.18149/MPM.5132023_14.

Introduction

The Welding Institute (TWI) created the Friction Stir Welding (FSW) method in 1991 as a revolutionary solid-joining process [1]. It offers a number of advantages over conventional fusion joining techniques, including no melting of the weld surfaces, welding of different materials, and reduction of various associated flaws, such as solidification cracking, deformation, porosity, and flash generation [2,3]. Aerospace, shipbuilding, automobile, and railway industries have utilised it extensively for butt and lap welding of aluminium alloys, magnesium alloys, copper alloys, etc., [4–7].

In FSW, a revolving tool (with a shoulder and a pin) is progressively introduced into the workpiece until the shoulder of the tool makes contact with the workpiece surface, as depicted

in Fig. 1. Due to frictional heating and plastic deformation, this posture is maintained until the necessary temperature is attained. To achieve the required weld, the instrument is moved along the weld line. AS refers to the side that has the same vectorial sense as the tangential velocity and tool traverse speed of a rotating tool. RS is the side with the opposite vectorial sense of the tangential velocity and tool traverse speed of a rotating tool [8]. The portion of the workpiece in front of the tool is referred to as the leading side, while the portion behind the tool is referred to as the trailing side (Fig. 1).

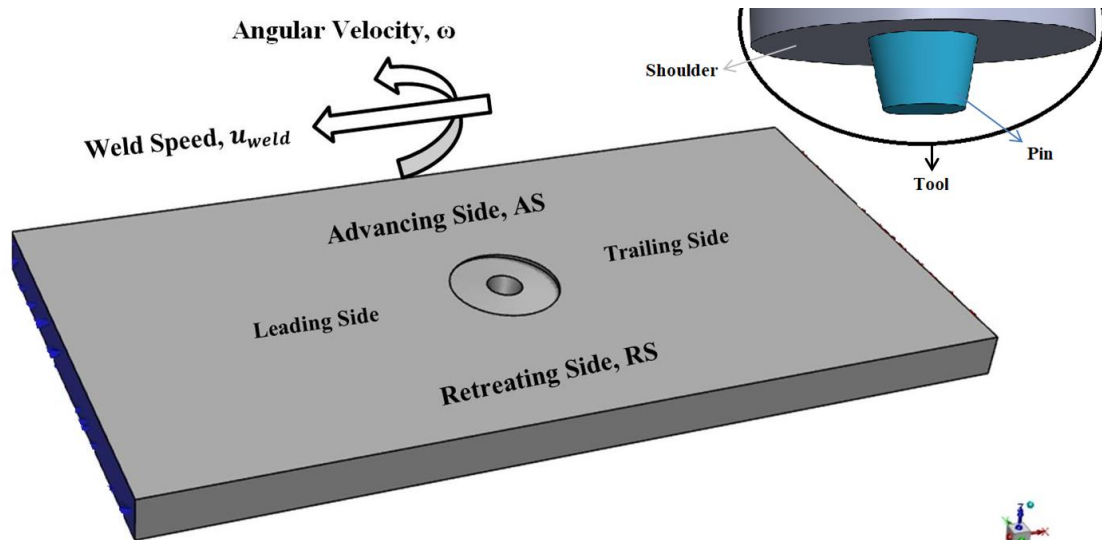


Fig. 1. Friction stir weld process

FSW is affected by the geometry of the tool, the weld speed, the rotating speed, the plunge depth, the tilt angle of the tool, and the weld materials. Each of these variables affects heat transmission and material flow, which in turn impacts the microstructure and quality of the weld [9,10]. Heat, temperature, and material flow are all impacted by the angle at which the tool is held [10]. As tool tilt angle is found to be one of the essential variables that impacts weld quality, this work focuses on evaluating its effect for a lap joint. In order to comprehend the effect of tool tilt angle, the present study employs the finite volume method (FVM) of CFD as a cost-effective and time-saving technique [11].

Literature Review

Several researchers have investigated FSW. C.M. Chen and Kovacevic [12] applied a 3D thermo-mechanical model to AA6061-T6 and determined that the largest temperature gradient in both the longitudinal and lateral directions occurred just beyond the shoulder edge. Nandan et al. [13–15] employed the visco-plastic 3D model to simulate FSW of stainless steel 304, aluminium alloy AA6061, and mild steel 1018, respectively. As a result of the rotational and linear motion of the instrument, their findings revealed a large asymmetry in the temperature profiles surrounding it. Z. Zhang [16] created a 3D thermo-mechanical model to investigate temperature and material flow on AA6061-T6. It was found that maximum temperature increases with rotating speed. Material particles on RS do not enter AS and are instead carried to the back of the rotating tool. Increasing the rotational speed and decreasing the welding speed increases the stirring motion, hence enhancing the quality of the weld. In order to prevent flaws, the rotation speed should rise in tandem with the welding speed. Using cellular automata linked finite element model (FEM) for AA6061 T6 material, Saluja, Narayanan, and Das [17] determined that the maximum temperature and strain rate occur near the weld center and decrease over the width of the weld. Keivani et al. [18] investigated the FEM of FSW on

Cu C11000. They discovered that when the pin angle increases, so does the temperature around the weld line, although preheating has a negligible effect on the temperature distribution. Darvazi and Iranmanesh [19] found that AS region had greater temperature than the RS, and this temperature difference was greater at the top side than underneath. In addition, plastic deformation generates higher heat at the tool-workpiece interface than in places further away. Also, temperature distribution was mainly due to heat convection coefficient. Pal and Phaniraj [20] used 3D CFD code for SS 304 work material using polycrystalline cubic boron nitride pin. They found that heat transferred to the workpiece is significantly higher (81 %) than retained with the tool. Also, temperature distribution along the circumference of the tool is almost constant at axial position. Jain, Pal, and Singh [21] used a 3D thermo-mechanical coupled model for butt welding of AA2024-T4. They noticed a greater material flow velocity in the frustum cone than in the cylindrical pin. Also, it was discovered that temperature increases with increasing rotating speed. Gao et al. [22] used FEM with tracer particle technique to study the material flow of AA6061. They found that upper surface material moves spirally downward due to shoulder movement and lower material first move spirally upward due to pin and then download. The material was collected on the advancing side after several rotations. They discovered that tracer particle velocity was greater at the tool's edge, and that the pin's stirring effect diminished beyond the pin's width. Also, more AS material entered into stir zone than the material on RS. Malik and Kailas [23] found that material flow was mainly shoulder driven and pin driven. For sound weld, a successful mix of both was required. Zhao et al. [24] used the 2D CFD model of butt FSW on AA6061. They observed that the temperature distribution was asymmetric, with a higher maximum temperature on AS than on RS. In addition, they noticed that material in front of the revolving tool moved in the direction of the tool's tangent. Zhang, Shi, et al. [25] developed a CFD model to investigate the impacts of tool tilt on heat transmission and material flow. They discovered that a tilted tool produced a higher temperature on the AS, a greater frictional force at the tool-workpiece interface (which enhances material flow behind the tool), and a vigorous stirring action. Chen et al. [26] investigated the effect of pin thread on FSW material flow. They discovered that a pin thread increases flow velocity and strain rate, traps material in a high-velocity zone, and creates the requisite vertical pressure gradient for top-to-bottom material flow. Zhang et al. [27] studied a CFD model of AA2024-T4 butt FSW. They discovered that sticking and sliding states coexist at the tool-workpiece contact, which affects the heat generation and distribution. Greatest frictional heat flux appeared at the shoulder's periphery, whereas maximum plastic deformation heat flux appeared at the tool's interior. The heat was not distributed uniformly. Meyghani, Awang, and Wu [28] noticed that material flow around the pin travels through the RS and stretches slightly in the direction of the AS. It was discovered that the shoulder elevates the material at the back of the tool. Also noted were an uneven temperature distribution near the weld's centerline and a high temperature on the AS.

Literature review reveals that there is no study that has considered tool tilt angle for CPCS to assess heat generation and material flow for a lap joint. The present work is an attempt in this direction. In the present research work, the influence of tool tilt angle (0, 1, 2, and 2.29 °) in lap joint arrangement with CPCS tool for Aluminum alloy AA6061 is evaluated. Solidworks® 2017 is used for the geometric modelling, while CFD software ANSYS® 19.3 R3 (FLUENT®) is employed for FVM numerical simulation [29]. By analysing temperature and velocity distribution, the effect of tool tilt angle on heat generation and material flow is evaluated.

from the workpiece surface. The following assumptions are used in line with the previous studies [10,11] in the present work:

1. Constant heat generation rate is assumed, i.e., a quasi-steady process.
2. Material that has been plasticized is categorized as a non-newtonian, incompressible, viscoplastic material.
3. No slip condition exists between the tool and the workpiece.
4. Free slip condition exists for upper, lower, and side surfaces of the workpiece.
5. Zero pressure value is assumed at the pressure outlet for the outlet boundary.
6. The material is assumed to behave as a non-newtonian fluid with temperature and strain rate dependent viscosity
7. Heat generation by the tool's shoulder side surface (SSS) is neglected in the simulation as it is non-significant in amount.

Table 2. Numbers of cells used in various cases

Name	Type	Number of Cells
Case 1	CPCS tool at 0 ° tilt angle	729,867
Case 2	CPCS tool at 1 ° tilt angle	912,254
Case 3	CPCS tool at 2 ° tilt angle	1,008,167
Case 4	CPCS tool at 2.29 ° tilt angle	2,407,607

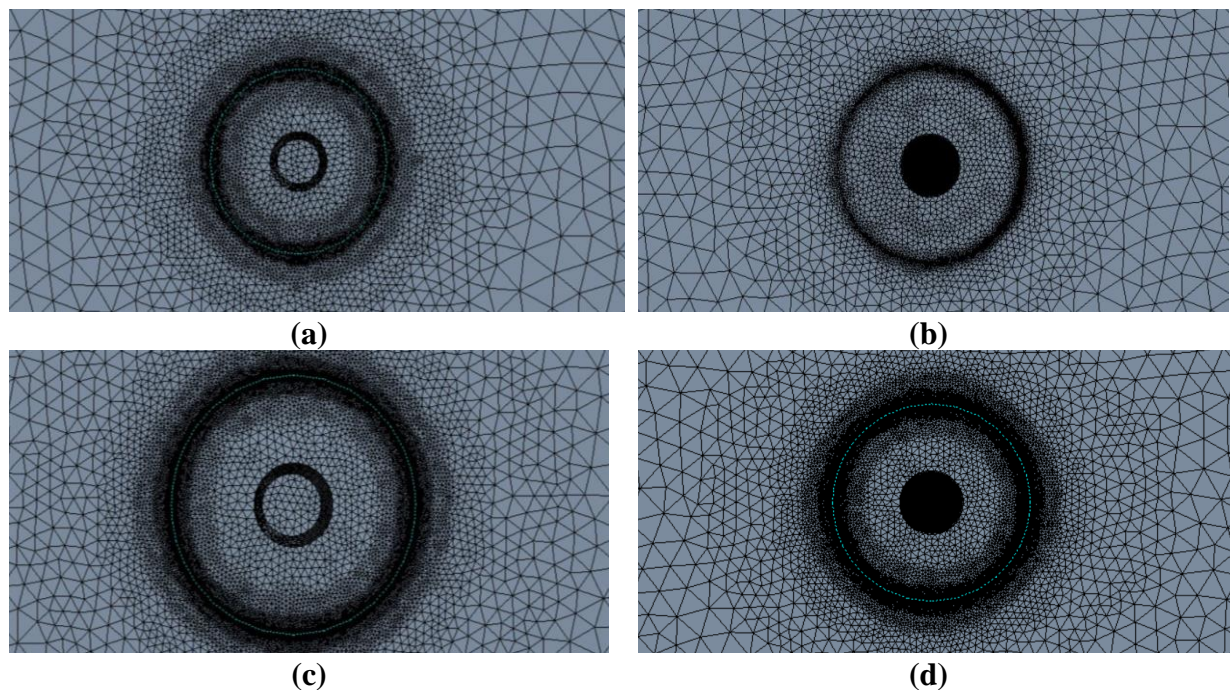


Fig. 3. Mesh used (a) Case 1, (b) Case 2, (c) Case 3, and (d) Case 4

Boundary Conditions and Material Properties. To accurately forecast welding performance, it is important to use realistic boundary conditions. The parts and boundary conditions of the model are presented in Fig. 4 [30].

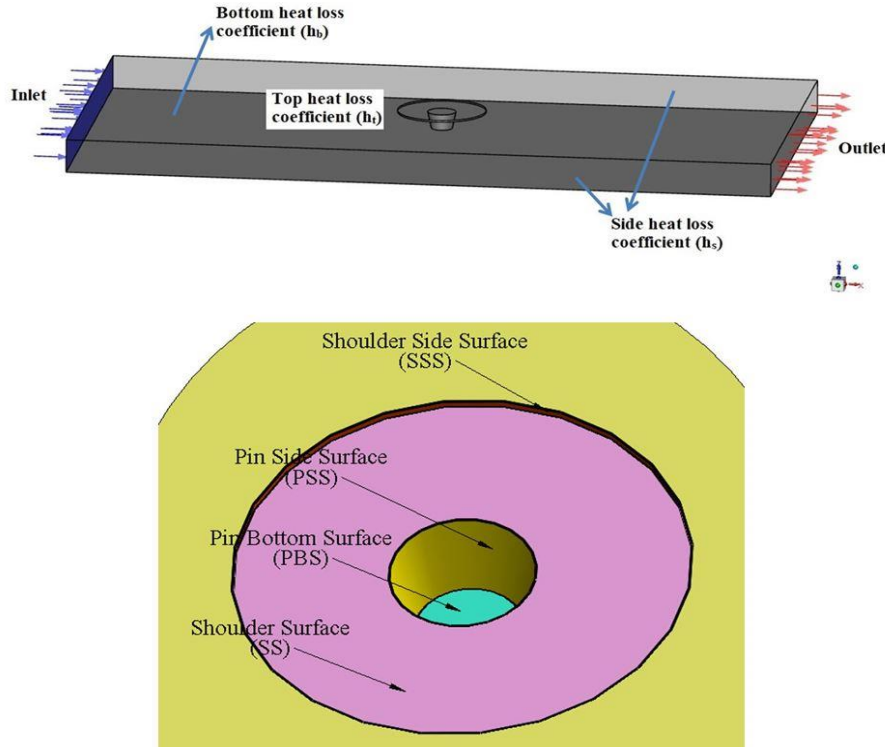


Fig. 4. Parts and Boundary conditions of the model

The flow boundary condition at the inlet is given below:

$$u = u_{weld}, v = 0, w = 0, \quad (1)$$

where welding velocity is denoted by u_{weld} , and the X , Y , and Z velocity intensities by u , v , and w , respectively.

Tool periphery velocity (resultant of tool angular velocity and welding speed) is given below:

$$u_i = \omega r \sin\theta - u_{weld}, v_i = \omega r \cos\theta, w_i = 0, \quad (2)$$

where r ranges such that $r_1 < r < r_3$. u_i , v_i and w_i represent velocity vectors in the X , Y , and Z directions, respectively. Index notation "i" represents a point on the tool surface at which resultant tool angular velocity and welding speed are calculated. r_1 is tool shoulder radius; r_3 is pin bottom radius; θ is the angle between the horizontal direction vector from tool axis to point on the cylindrical surface, and it is zero in the weld direction.

The viscosity (η), flow stress (σ), Zener-Hollomon parameter (Z), and strain rate ($\bar{\epsilon}$) are calculated from Equations (3), (4), (5), and (6) [31–33]:

$$\eta = \frac{\sigma}{3\bar{\epsilon}}, \quad (3)$$

$$\sigma = \frac{1}{\beta} \ln \left\{ \left(\frac{Z}{A} \right)^{\frac{1}{n}} + \left(1 + \left(\frac{Z}{A} \right)^{\frac{2}{n}} \right)^{\frac{1}{2}} \right\}, \quad (4)$$

$$Z = \bar{\epsilon} e^{\left(\frac{Q}{RT} \right)}, \quad (5)$$

$$\bar{\epsilon} = \left(\frac{2}{3} \epsilon_{ij} \epsilon_{ij} \right)^{\frac{1}{2}}, \quad (6)$$

where T (in K) is temperature. Both temperature and strain rate are read automatically via the FLUENT® code. A , β , and n are material constants; Q is temperature independent activation energy; R is gas constant. In FLUENT® software, viscosity Equation (3) is implemented using User Defined Functions (UDF).

The material constants and properties for AA6061 Aluminum alloy (with prior history of Direct Chill Cast (DCC) and Homogenisation (H)) are presented in Table 3 [34].

Table 3. Material (AA6061-T6) constants and properties

Parameter	Value
Material constants:	
A	$2.41 \times 10^8 \text{ (s}^{-1}\text{)}$
n	3.55
Q	$1.45 \times 10^5 \text{ (J}\cdot\text{mol}^{-1}\text{)}$
β	0.045 (MPa)
Material density, ρ	$2700 \text{ (kg}\cdot\text{m}^{-3}\text{)}$
Gas constant, R	$8.314 \text{ (J}\cdot\text{K}^{-1}\cdot\text{mol}^{-1}\text{)}$

The heat generated in FSW process appears in different areas. The surface of the tool that contacts the workpiece has been divided into three parts: shoulder surface (SS), pin side surface (PSS), and pin bottom surface (PBS) as shown in Fig. 4. The heat generated by various sources is given below:

$$Q_{total} = \delta Q_{sticking} - (1 - \delta)Q_{sliding}, \quad (7)$$

where δ is contact state variable. When $\delta = 0$ (slip), heat is generated only by friction. When $\delta = 1$ (stick), all heat is generated by plastic material deformation [35].

The maximum shear stress for yielding is assumed to be:

$$\tau_b = \frac{\sigma_s}{\sqrt{3}}, \quad (8)$$

where σ_s is material yield stress (at melting point temperature) [36].

The SS is further divided into conical shoulder surface (CSS) and flat shoulder surface (FSS). Shoulder-workpiece interface has partial sticking-sliding contact [11]. The value for the contact state variable at CSS and FSS has been taken as 0.35. The heat flux (W/m^2) at the CSS, FSS, and SSS is given below:

$$q_{CSS} = \frac{[\delta_{CSS}\tau_b + (1 - \delta_{CSS})\mu P]2\omega[(r_1^3 - r_2^3)(1 + \tan\alpha')]}{3(r_1^2 - r_2^2)}. \quad (9)$$

Tool pin side and workpiece interface has partial sticking-sliding contact, with 0.5 as value for the contact state variable at pin side surface (PSS). The heat flux (W/m^2) at PSS is given by Equation (10), where α is the pin cone angle [11]:

$$q_{PSS} = \frac{2\delta_{PSS}\omega\tau_b(r_2^3 - r_3^3)\cos\alpha}{3(r_2^2 - r_3^2)} + \frac{2(1 - \delta_{PSS})\mu P\omega(r_2^3 - r_3^3)}{3(r_2^2 - r_3^2)}. \quad (10)$$

Tool pin bottom and workpiece interface has partial sticking-sliding contact with 0.35 as the value for contact state variable at PBS. The heat flux (W/m^2) at PBS is given below [11]:

$$q_{PBS} = \frac{2\omega r_3(\delta_{PBS}\tau_b + (1 - \delta_{PBS})\mu P)}{3}, \quad (11)$$

where μ is friction coefficient (assumed to be 0.4)[11]; P is plunging pressure (Pa); ω is tool angular velocity (rad/s) and α' is shoulder cone angle (α' is zero for flat shoulder surface (FSS)). A plunge pressure of 12 MPa is used [11].

Specific heat (C_p) and thermal conductivity (k) of AA6061 weld material are represented by Equations (12) and (13), respectively [14].

$$C_p = 929 - 0.627T + 1.481 \times 10^{-3}T^2 - 4.33 \times 10^{-8}T^3, \quad (12)$$

$$k = 25.22 + 0.3978T + 7.358 \times 10^{-6}T^2 - 2.518 \times 10^{-7}T^3. \quad (13)$$

The heat exchange boundary condition between the workpiece's top surface and the environment is convective heat transfer [14]. The heat exchange boundary condition for the workpiece's top, bottom, and side surfaces are given by Equations (14), (15), and (16), respectively [14].

$$k \frac{\partial T}{\partial z} = h_t(T - T_0), \tag{14}$$

$$k \frac{\partial T}{\partial z} = h_b(T - T_0), \tag{15}$$

$$k \frac{\partial T}{\partial z} = h_s(T - T_0), \tag{16}$$

where h_t is heat dissipation coefficient at the top surface. h_b and h_s are heat loss coefficients at bottom surface and side surface, respectively ($h_b = h_s$) and T_0 is ambient temperature (300 K).

In this study, h_t is 30 W/m²K [11]. The heat loss coefficient for the workpiece's bottom surface and side surface ($h_b = h_s$) is 500 W/m²K [11].

Model Validation. CFD model was validated against the work by [11]. The results for temperature distribution and material flow velocity are in close agreement with the results as reported by them. Figure 5 shows the result comparison of temperature distribution for the current study with the validated one. Thus, the methodology and procedure used for numerical simulation are found to be satisfactory.

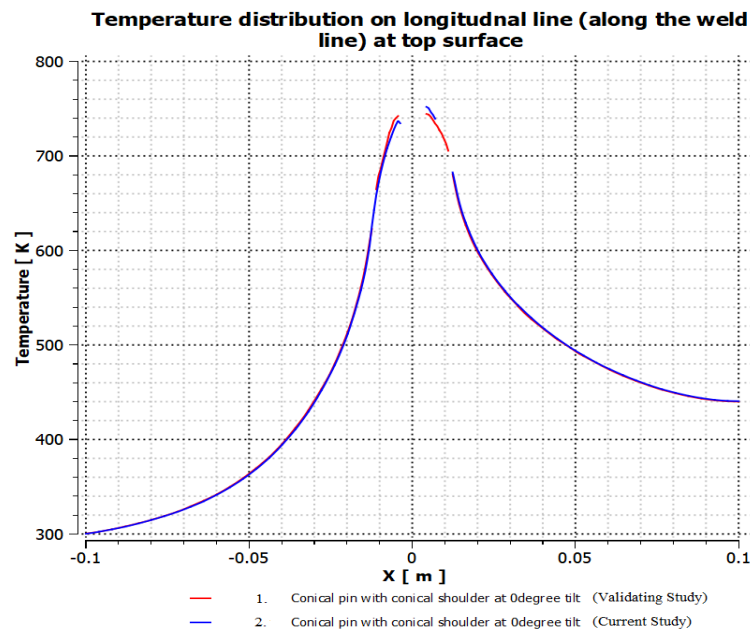
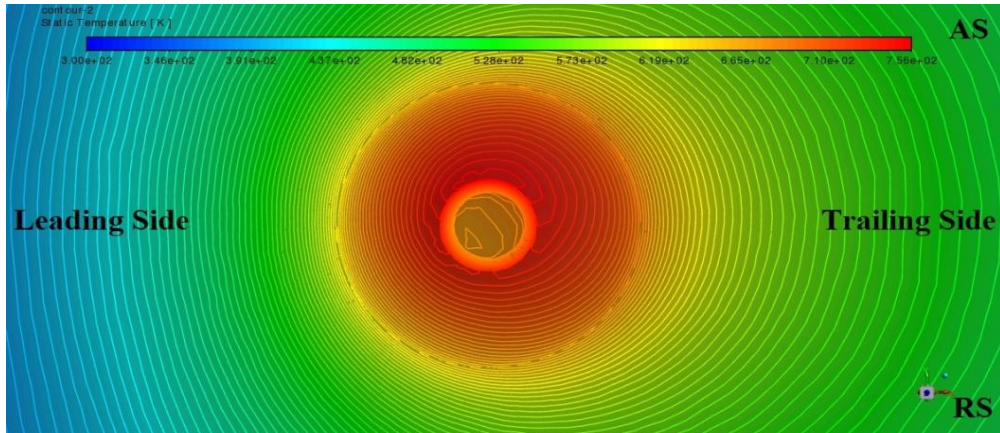


Fig. 5. Temperature distribution comparison for the current study with the validating study

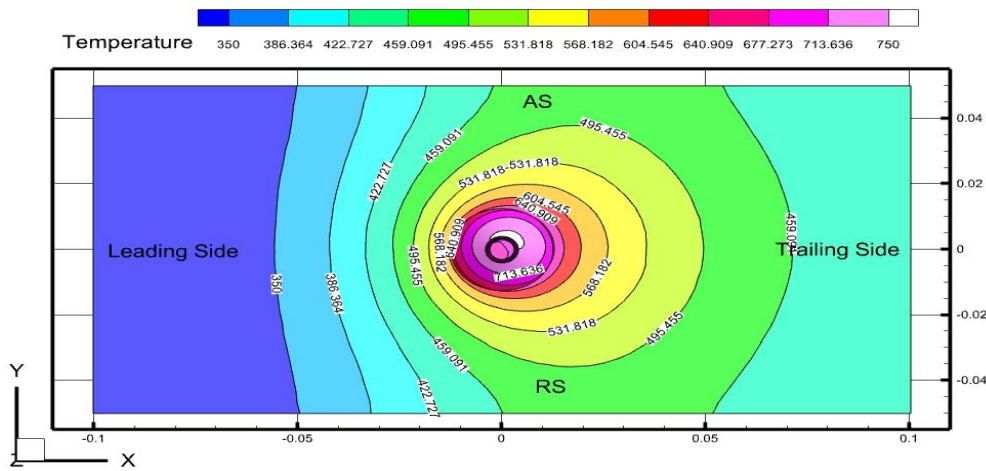
Results and Discussion

This section discusses the effect of tool tilt angle on temperature distribution and material flow.

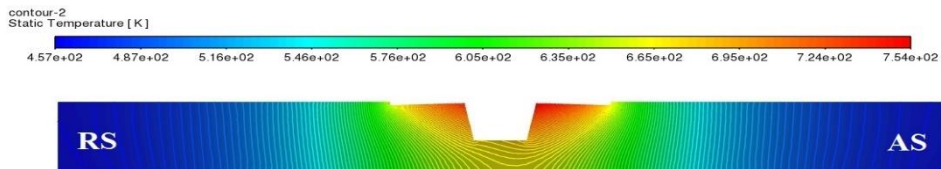
Effect of Tilt Angle on Temperature Distribution. Temperature distribution for CPCS at 0° tilt angle is shown in Figs. 6(a-d). Temperature contour lines are the lines drawn to show the equal temperature, which means that the temperature remains constant when the contour line is followed. Contour lines show valleys and hills and the steepness or gentleness of slopes. The gradient of the contour function (here, temperature) is always perpendicular to the contour lines. If the temperature contour lines are close together, it represents a steep temperature slope (i.e., the magnitude of the temperature gradient is large). If temperature contours have wide spaces, the variation of temperature is relatively flat (i.e., the magnitude of the temperature gradient is small). The contour interval of the contour map shows the temperature difference between the successive contour lines.



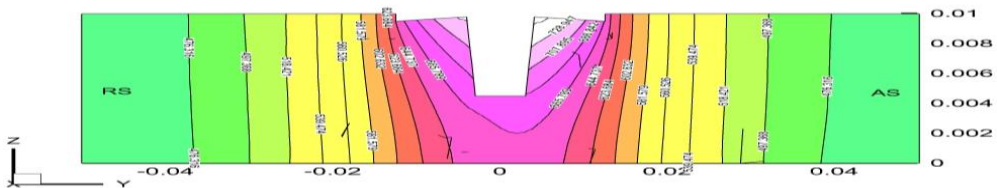
(a)



(b)



(c)



(d)

Fig. 6. Temperature distribution for conical pin tool with a conical shoulder at 0° tilt angle:
 (a) tool-workpiece interface's top view in FLUENT[®] post processing;
 (b) tool-workpiece interface's top view using Tecplot[®];
 (c) transverse view of the tool-workpiece interface in FLUENT[®] post-processing;
 (d) transverse view of the tool-workpiece interface using Tecplot[®]

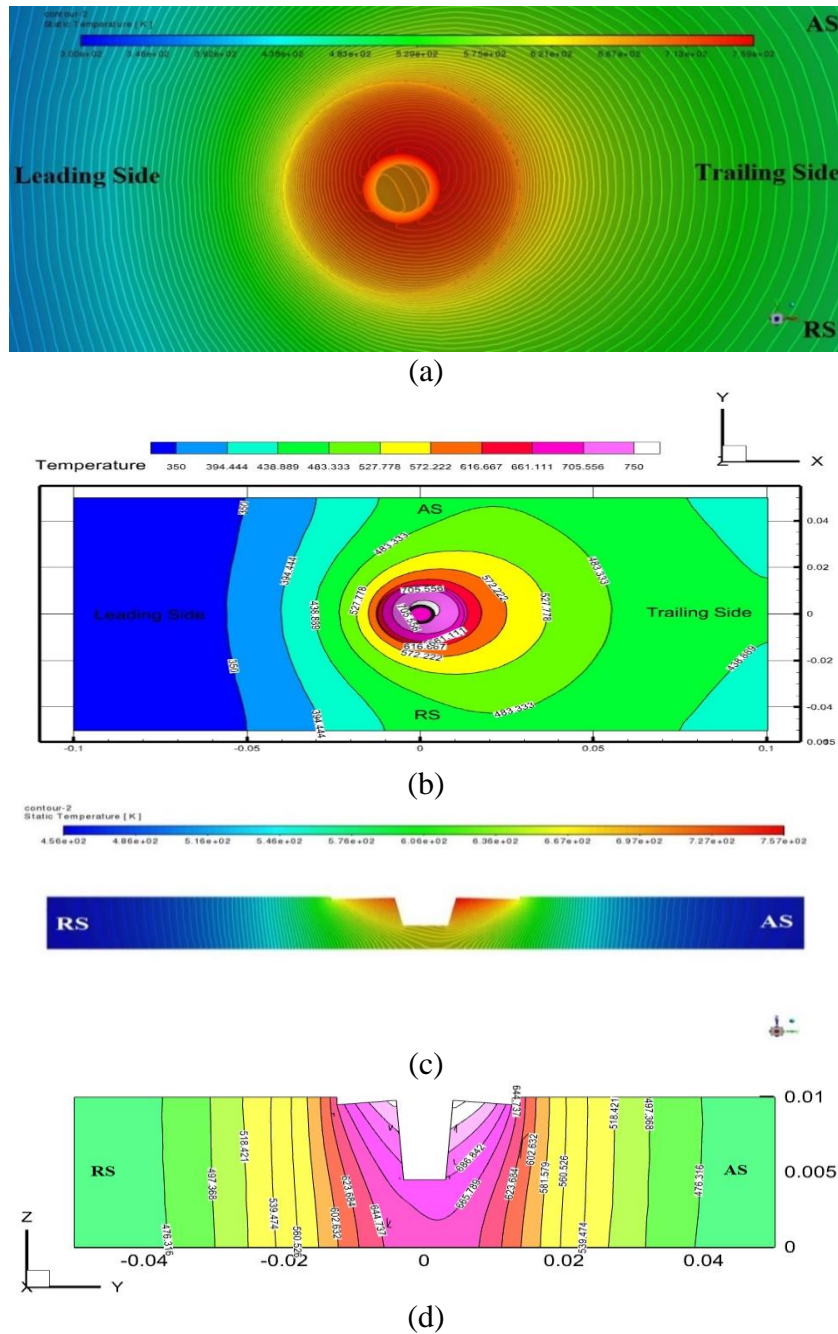
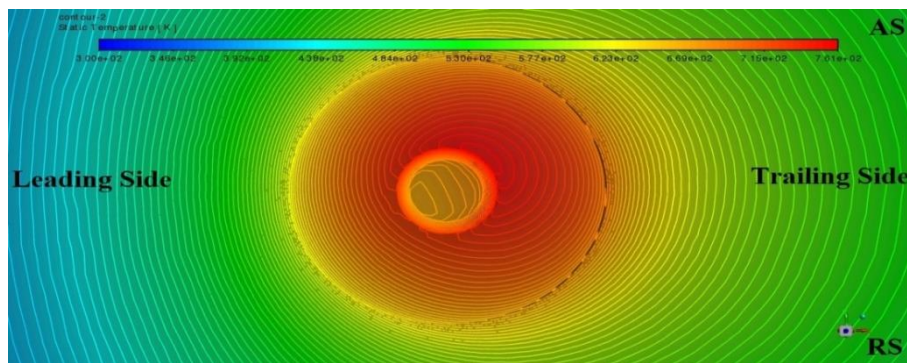


Fig. 7. Temperature distribution for conical pin tool with a conical shoulder at 1 ° tilt angle:
 (a) tool-workpiece interface's top view in FLUENT® post-processing;
 (b) tool-workpiece interface's top view using Tecplot®;
 (c) transverse view of the tool-workpiece interface in FLUENT® post processing;
 (d) transverse view of the tool-workpiece interface using Tecplot®

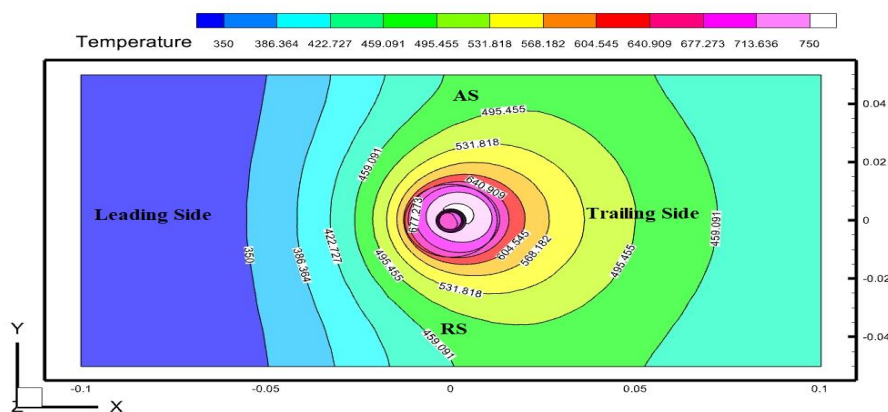
Figure 5(a) indicates that peak temperature generated is 756 K. Further, high-temperature contour lines for CSS are situated on trailing AS of the shoulder. This means that temperature variation is less steep on trailing AS as the gradient of temperature is less in this region, resulting in a gradual temperature slope here. On the trailing side of the tool, the temperature contour lines are more widely separated than on the leading side, and it indicates relatively flat temperature variation, i.e., a small temperature gradient. The temperature generated on the transverse plane of the tool-workpiece interface is in the range of 457-754 K (Fig. 5(c)). In the transverse plane, temperature contour lines are oriented towards the AS,

meaning temperature variation is less steep on the AS as the gradient of temperature is less in this region, resulting in a gradual temperature slope on this side.

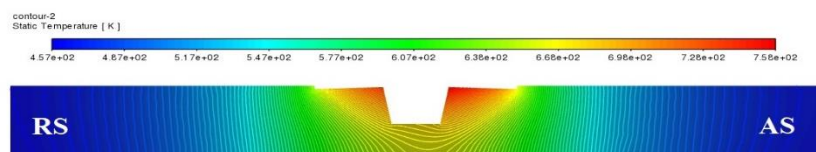
Figure 7(a) depicts temperature distribution for CPCS at a 1° tilt angle. It indicates that the maximum temperature produced is 759 K. The temperature produced on the transverse plane of the tool-workpiece interface ranges between 456 and 757 K (Fig. 7(c)). Temperature contour lines in the transverse plane are oriented towards AS. When a tool tilt angle of 1° is used, there is an increase in peak temperature generated in the workpiece. In addition, the transverse plane's peak temperature rises.



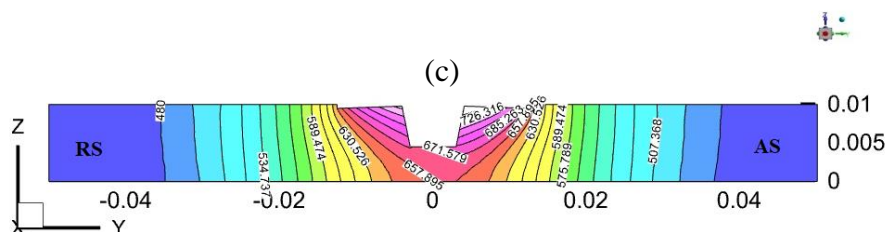
(a)



(b)



(c)



(d)

Fig. 8. Temperature distribution for conical pin tool with a conical shoulder at 2° tilt angle:

- (a) tool-workpiece interface's top view in FLUENT[®] post processing;
- (b) tool-workpiece interface's top view using Tecplot[®];
- (c) transverse view of the tool-workpiece interface in FLUENT[®] post-processing;
- (d) transverse view of the tool-workpiece interface using Tecplot[®]

Temperature distribution for CPCS at a 2° tilt angle is shown in Figs. 8(a-d). The peak temperature generated is 761 K (Fig. 8(a)). The temperature produced on the transverse plane of the tool-workpiece interface ranges between 457 and 758 K (Fig. 8(c)). When compared to the previous two cases, the workpiece generates a higher peak temperature. The peak temperature on the transverse plane also increases by 4 K when compared with tool tilt angle of 0°, and it increases by 1 K when compared with 1° tool tilt angle. This indicates that the peak temperature increases as the tool tilt angle rises.

Temperature distribution for CPCS at a 2.29° tilt angle is shown in Figs. 9(a,b). The peak temperature generated is the same as that of 2° tilt angle case (Fig. 9 (a)). The temperature produced on the transverse plane of the tool-workpiece interface is also the same as that of 2° tilt angle case (Fig. 9(b)). This is due to the fact that tilt angles of 2° and 2.29° are too close to show the temperature difference.

As a result, it is safe to conclude that as the tool tilt angle increases, so does the peak temperature.

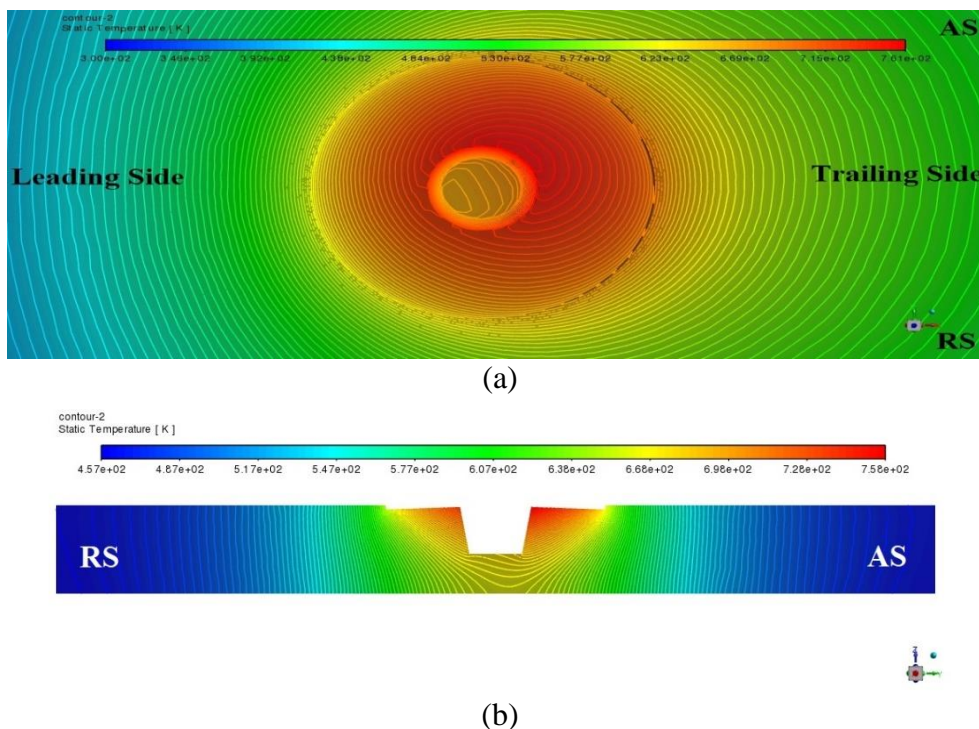


Fig. 9. Temperature distribution for conical pin tool with a conical shoulder at 2.29° tilt angle:
 (a) tool-workpiece interface's top view in FLUENT® post-processing;
 (b) transverse view of the tool-workpiece interface in FLUENT® post-processing

General observations made during the study are written below:

1. The high-temperature contour lines are situated on trailing AS of the shoulder, as shown in Figs. 6-9. This means that temperature variation is less steep on the trailing AS as temperature gradient is smaller in this region, resulting in a gradual temperature slope here. This is validated by the fact that trailing AS experiences a high shearing rate and velocity, and it results in higher plastic strain and hence more heat generation.
2. On the trailing side of the tool, the temperature contour lines are more widely separated than on the leading side, as shown in Figs. 6(a), 7(a), 8(a), and 9(a), and it indicates relatively flat temperature variation, i.e., a small temperature gradient.
3. In the transverse plane, temperature contour lines are oriented towards the AS, as shown in Figs. 6(c,d), 7(c,d), 8(c,d), and 9(b). This means temperature variation is less steep on the

AS as the gradient of temperature is less in this region, resulting in a gradual temperature slope on this side.

4. The temperature contour lines on the transverse plane are denser at the top and widely spaced at the bottom of the workpiece along the thickness, as shown in Figs. 6(c,d), 7(c,d), 8(c,d), and 9(b). This means that the temperature gradient decreases from top to bottom along the workpiece thickness. This is validated by the fact that the generation of heat is maximum along the region close to the tool shoulder, and the convection coefficient is maximum between the workpiece-backing plate interface.

5. The numerical model is also validated by the fact that the maximum temperature generated in all the cases of the present study is lower than the solidus temperature of the workpiece material (AA6061), as shown in Figs. 6(a), 7(a), 8(a) and 9(a), and it is a necessary condition for a good friction stir weld [11].

6. The temperature generation along the thickness of both plates is higher than recrystallization temperature but less than melting point temperature, as shown in Figs. 6(d), 7(d), 8(d), and 9(b), which is required for proper welding in FSW. Thus, the given model is further verified.

Tilt Angle's Impact on Material Flow. Figures 10(a,c) represent velocity contour and particle streamlines on the longitudinal plane along the weld line for CPCS at 0° tilt angle, respectively. Peak magnitude of velocity produced is 0.749 m/s and its range at tool-workpiece interface is 0.0311-0.749 m/s. Figures 10(a,b) indicate that the magnitude of velocity increases with radius and is maximum at the outer periphery for all the surfaces of the tool-workpiece interface. Further, particle streamlines are irregular, as shown in Fig. 10(c).

Figure 11(a,b) shows velocity contour and particle streamlines on the longitudinal plane along the weld line for CPCS at 1° tilt angle. The maximum velocity produced is 0.750 m/s, with a range of 0.00414-0.750 m/s at the tool-workpiece interface, as shown in Fig. 11(a). On comparing Fig. 11(b) with Fig. 10(c), it is found that particle streamlines are less regular than in CPCS tool at 0° tilt angle.

Figure 12(a,b) depict velocity contour and particle streamlines on the longitudinal plane along the weld line for a CPCS with a 2° tilt angle. The maximum velocity produced is 0.750 m/s, with a range of 0.0342 to 0.750 m/s at the tool-workpiece interface, as shown in Fig. 12(a). Figure 12(b) indicates that particle streamlines are more irregular than in the preceding case of 0° and 1° tilt angles.

Figure 13(a,b) depict velocity contour and particle streamlines on the longitudinal plane along the weld line for a CPCS with a 2.29° tilt angle. The maximum velocity produced is same as that of 2° tilt angle case, as shown in Fig. 13(a). Particle streamlines show same behavior as that of 2° tilt angle case, as shown in Fig. 13(b). This is due to the fact that tilt angles of 2° and 2.29° are too close.

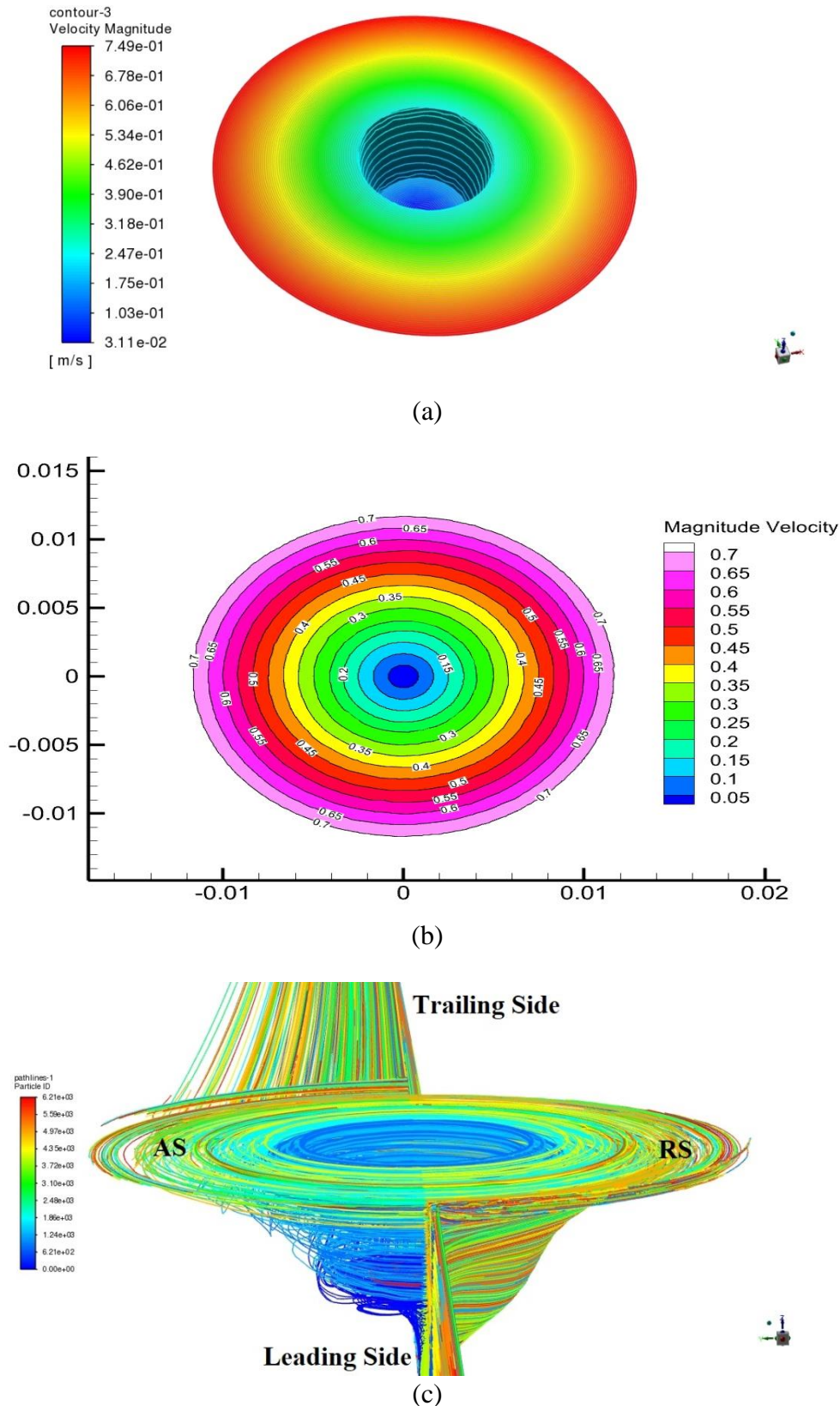
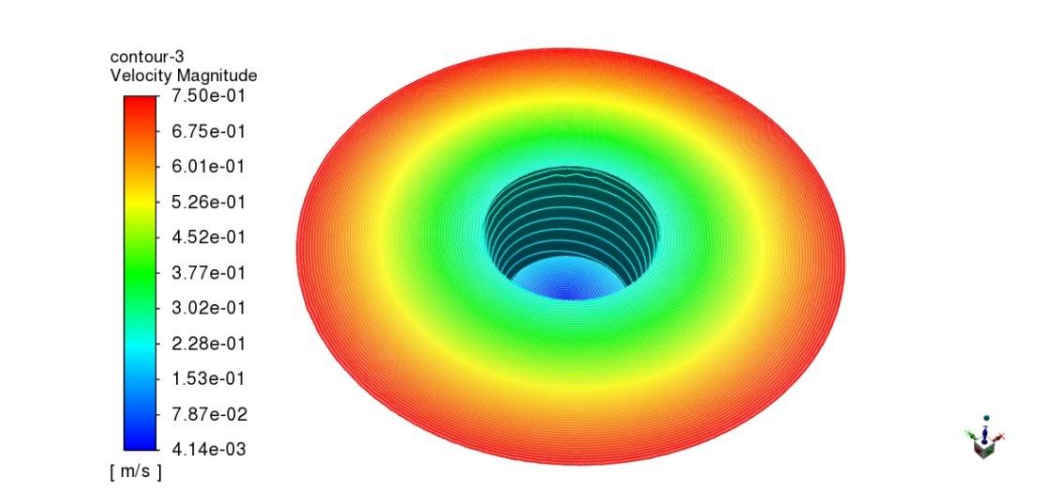
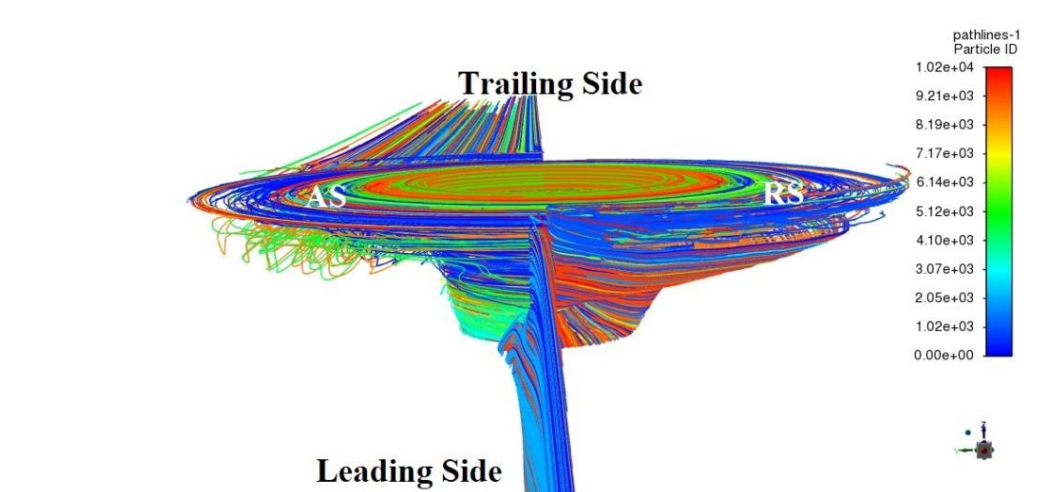


Fig. 10. Conical pin tool with a conical shoulder at 0° tilt angle: (a) velocity contour at the tool-workpiece interface in FLUENT® post-processing (b) contour of velocity at tool and workpiece interface using Tecplot®; (c) particle streamlines on the longitudinal plane along the weld line in FLUENT® post-processing

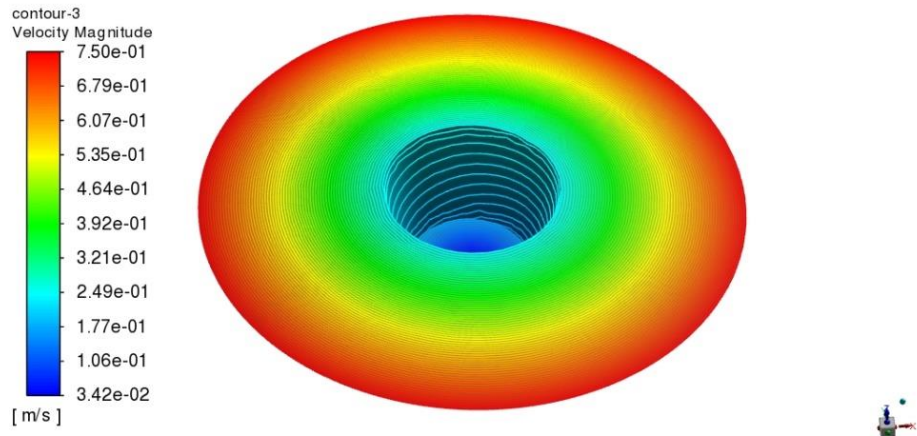


(a)

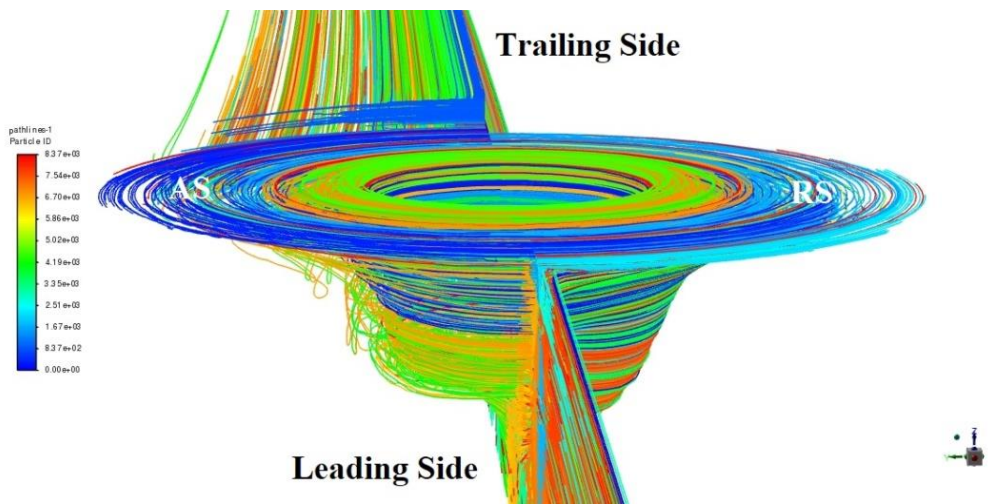


(b)

Fig. 11. Conical pin tool with a conical shoulder at 2° tilt angle:
 (a) velocity contour at the tool-workpiece interface in FLUENT[®] post-processing;
 (b) particle streamlines on the longitudinal plane along the weld line in FLUENT[®] post-processing



(a)



(b)

Fig. 12. Conical pin tool with a conical shoulder at 2° tilt angle:
(a) velocity contour at the tool-workpiece interface in FLUENT® post-processing;
(b) particle streamlines on the longitudinal plane along the weld line in FLUENT® post-processing

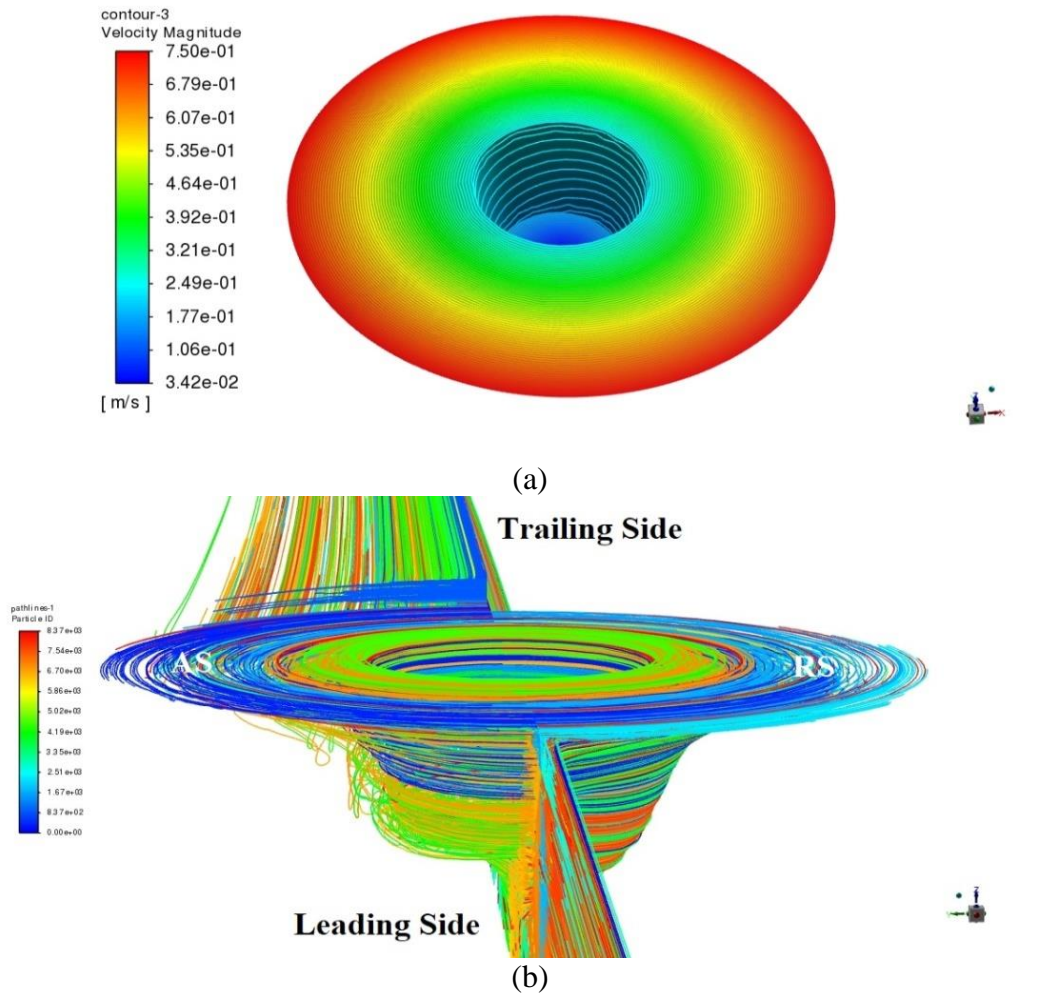


Fig. 13. Conical pin tool with a conical shoulder at 2.29° tilt angle:
 (a) velocity contour at the tool-workpiece interface in FLUENT® post-processing;
 (b) particle streamlines on the longitudinal plane along the weld line in FLUENT® post-processing

General observations made during the material flow study are written below:

1. The flow of material takes place in the region close to the tool. Since, in the present paper, the stick condition is assumed between tool-workpiece interface, material velocity is approximately equal to the linear velocity of the tool. This is shown in Figs. 10(a,b), 11(a), 12(a) and 13(a).
2. The flow of material is found to be weakest in the region close to the pin bottom, as shown in Figs. 10(a,b), 11(a), 12(a), and 13(a). It is also noticed that magnitude of velocity increases with radius and is maximum at the outer periphery for all the surfaces of the tool-workpiece interface.
3. Peak velocity magnitude remains the same when the tool tilt angle is increased from 0 to 2.29° tilt angle, as shown in Figs. 10(a,b), 11(a), 12(a), and 13(a).
4. Regular streamlines are observed at 0° tool tilt angle, but irregular streamlines are observed at 1 and 2° tool tilt angle. Further, streamlines are denser at the RS, and the material flow gets expanded at the trailing side as tool tilt angle is provided on the trailing side. This is shown in Figs. 10(c), 11(b), 12(b) and 13(b).
5. Figures 10(c), 11(b), 12(b), and 13(b) show that material on the leading AS and tool front is swept along the RS to get deposited at the tool back.

6. At a tool tilt angle of 0° , horizontal streamlines are detected, and at 1° , 2° , and 2.29° tool tilt angles, scattered streamlines with leading side tilt in the vertical direction are observed. This is shown in Figs. 10(c), 11(b), 12(b) and 13(b).

Conclusions

This investigation considers a CPCS tool at four distinct tilt angles (0° , 1° , 2° , and 2.29°) to examine how the tilt angle of the tool impacts heat transfer and material flow. The following conclusions can be drawn from the study:

- The high-temperature contour lines lean more towards the AS as the tool tilt angle is increased from 0° to 2.29° , as indicated in Cases 2, 3, and 4.
- At the transverse plane, temperature contour lines lean more towards the AS as the tilt angle is increased from 0° to 2.29° .
- Results indicate that higher temperature is generated on the trailing AS, high-temperature gradient on the leading side of the tool, maximum heat generation occurs near the tool shoulder, and temperature decreases from top to bottom surface along the workpiece thickness.
- As the tilt angle is increased from 0° to 2.29° , the peak temperature increases from 756 K to 761 K in the CPCS tool.
- For the CPCS tool, the effect of tilt angle on the amplitude of the peak velocity is negligible. At 0° tool tilt angle, horizontal streamlines are detected, and at 1° , 2° , and 2.29° tool tilt angles, scattered streamlines with leading side tilt in the vertical direction are observed.
- The material from the leading AS and the front of the tool is swept along the RS and deposited at the back of the tool.

Thus, it can be deduced that for CPCS, if the tilt angle of the tool is raised, the peak temperature will likewise increase, but the peak material velocity will remain the same.

References

1. Tsang S. Friction welding. In: *Welding, Brazing, and Soldering*. ASM International; 1993.
2. Singh BR. *A Hand Book on Friction Stir Welding*. UK: LAP Lambert Academic Publishing; 2012
3. Soleymani S, Abdollah-Zadeh A, Alidokht SA. Microstructural and tribological properties of ultra fine grained hybrid composite produced by friction stir processing. *Mater. Phys. Mech.* 2013;17(1): 6–10.
4. Zhao J, Jiang F, Jian H, Wen K, Jiang L, Chen X. Comparative investigation of tungsten inert gas and friction stir welding characteristics of Al-Mg-Sc alloy plates. *Mater. Des.* 2010;31(1): 306–311.
5. Cavaliere P, Cabibbo M, Panella F, Squillace A. 2198 Al-Li plates joined by Friction Stir Welding: Mechanical and microstructural behavior. *Mater. Des.* 2009;30(9): 3622–3631.
6. Thomas W, Nicholas E. Formability of friction stir welded dual phase steel sheets. In: *Frict Stir Weld Process III - Proc a Symp Spons by Shap Form Comm Miner Met Mater Soc TMS*. 1997. p.91–96.
7. Lebaal N, Chamoret D, Schlegel D, Folea M. Thermal modelling of Friction Stir Process (FSP) and identification parameters. *Mater. Phys. Mech.* 2017;32(1): 14–20.
8. Nandan R, DebRoy T, Bhadeshia HKDH. Recent advances in friction-stir welding - Process, weldment structure and properties. *Prog. Mater. Sci.* 2008;53(6): 980–1023.
9. Sun Z, Wu CS, Kumar S. Determination of heat generation by correlating the interfacial friction stress with temperature in friction stir welding. *J. Manuf. Process.* 2018;31: 801–811.
10. Zhai M, Wu CS, Su H. Influence of tool tilt angle on heat transfer and material flow in

- friction stir welding. *J. Manuf. Process.* 2020;59: 98–112.
11. Zhang J, Shen Y, Li B, Xu H, Yao X, Kuang B, Gao J. Numerical simulation and experimental investigation on friction stir welding of 6061-T6 aluminum alloy. *Mater. Des.* 2014;60: 94–101.
 12. Chen CM, Kovacevic R. Finite element modeling of friction stir welding — thermal and thermomechanical analysis. *International Journal of Machine Tools and Manufacture.* 2003;43(13): 1319–1326.
 13. Nandan R, Roy GG, Lienert TJ, Debroy T. Numerical modelling of 3D plastic flow and heat transfer during friction stir welding of stainless steel. *Sci. Technol. Weld Join.* 2006;11(5): 526–537.
 14. Nandan R, Roy GG, Debroy T. Numerical simulation of three dimensional heat transfer and plastic flow during friction stir welding. *Metall. Mater. Trans. A.* 2006;37(4): 1247–1259.
 15. Nandan R, Roy GG, Lienert TJ, Debroy T. Three-dimensional heat and material flow during friction stir welding of mild steel. *Acta Mater.* 2007;55(3): 883–895.
 16. Zhang Z, Zhang HW. Numerical studies on controlling of process parameters in friction stir welding. *J. Mater. Proc. Tech.* 2009;209(1): 241–270.
 17. Saluja RS, Narayanan RG, Das S. Cellular automata finite element (CAFE) model to predict the forming of friction stir welded blanks. *Comput. Mater. Sci.* 2012;58: 87–100.
 18. Keivani R, Bagheri B, Sharifi F, Ketabchi M, Abbasi M. Effects of pin angle and preheating on temperature distribution during friction stir welding operation. *Trans. Nonferrous. Met. Soc. China.* 2013;23(9): 2708–2713.
 19. Darvazi AR, Iranmanesh M. Prediction of asymmetric transient temperature and longitudinal residual stress in friction stir welding of 304L stainless steel. *J. Mater.* 2014;55: 812–820.
 20. Pal S, Phaniraj MP. Determination of heat partition between tool and workpiece during FSW of SS304 using 3D CFD modeling. *J. Mater. Process. Technol.* 2015;222: 280–286.
 21. Jain R, Pal SK, Singh SB. A study on the variation of forces and temperature in a friction stir welding process : A finite element approach. *J. Manuf. Process.* 2016;23: 278–286.
 22. Gao E, Zhang X, Liu C, Ma Z. Numerical simulations on material flow behaviors in whole process of friction stir welding. *Trans. Nonferrous. Met. Soc. China.* 2018;28(11): 2324–2334.
 23. Malik V, Kailas S V. Plasticine modeling of material mixing in friction stir welding. *J. Mater. Process. Tech.* 2018;258: 80–88.
 24. Zhao P, Shen Y, Huang G, Zheng Q . Numerical simulation of friction stir butt-welding of 6061 aluminum alloy. *Trans. Nonferrous. Met. Soc. China.* 2018;28(6): 1216–1225.
 25. Zhang S, Shi Q, Liu Q, Xie R, Zhang G, Chen G. Effects of tool tilt angle on the in-process heat transfer and mass transfer during friction stir welding. *Int. J. Heat. Mass. Transf.* 2018;125: 32–42.
 26. Chen G, Li H, Wang G, Guo Z, Zhang S, Dai Q, Wang X, Zhang G, Shi Q. Effects of pin thread on the in-process material flow behavior during friction stir welding: A computational fluid dynamics study. *Int. J. Mach. Tools. Manuf.* 2018;124: 12–21.
 27. Zhang S, Chen G, Liu Q, Li H, Zhang G, Wang G, Shi Q. Numerical analysis and analytical modeling of the spatial distribution of heat flux during friction stir welding. *J Manuf Process.* 2018;33: 245–255.
 28. Meyghani B, Awang M, Wu CS. Finite element modeling of friction stir welding (FSW) on a complex curved plate. *J. Adv. Join. Proc.* 2020;1: 100007.
 29. Kumar A, Bansal SN, Chandraker R. Computational modeling of blast furnace cooling stove based on heat transfer analysis. *Mater. Phys. Mech.* 2012;15(1): 46–65.
 30. Hasan AF. CFD modelling of friction stir welding (FSW) process of AZ31 magnesium

- alloy using volume of fluid method. *J. Mater. Res. Technol.* 2019;8(2): 1819–1827.
31. Thomas WM, Johnson KI, Wiesner CS. Friction stir welding-recent developments in tool and process technologies. *Adv. Eng. Mater.* 2003;5(7): 485–490.
 32. Sheppard T, Wright DS. Determination of flow stress: Part 1 constitutive equation for aluminium alloys at elevated temperatures. *Metals Technology.* 1979;6(1): 215-223.
 33. Sheppard T, Jackson A. Constitutive equations for use in prediction of flow stress during extrusion of aluminium alloys. *Materials Science and Technology.* 1997;13(3): 203-209.
 34. Tello KE, Gerlich AP, Mendez PF. Constants for hot deformation constitutive models for recent experimental data. *Sci Technol Weld Join.* 2010;15(3): 260–266.
 35. Hamilton C, Dymek S, Sommers A. A thermal model of friction stir welding in aluminum alloys. *Int. J. Mach. Tools Manuf.* 2008;48(10): 1120–1130.
 36. Neto DM, Neto P. Numerical modeling of friction stir welding process: A literature review. *Int. J. Adv. Manuf. Technol.* 2013;65(1–4): 115–126.

THE AUTHORS

Amit Yadav 
e-mail: amit.insan77@gmail.com

Ajai Jain
e-mail: ajayjainfme@nitkkr.ac.in

Rajiv Verma
e-mail: rajivkkr@nitkkr.ac.in